AGU100 ADVANCING EARTH AND SPACE SCIENCE

Geochemistry, Geophysics, Geosystems

RESEARCH ARTICLE
10.1029/2019GC008728

Key Points:
- Magnetite close to the superparamagnetic-single domain transition does not produce consistent or accurate paleointensity results
- Grain-size distributions containing only stable single domain magnetite in the Tiva Canyon Tuff produce high-quality, consistent paleointensity results
- Post-emplacement hydration or alteration does not appear to influence results here but should always be considered

Supporting Information:
- Supporting Information S1
- Figure S1
- Figure S2
- Figure S3
- Figure S4

Correspondence to:
F. Abdulghafur,
fatimah.ilimpen@gmail.com

Citation:
Abdulghafur, F., & Bowles, J. A. (2019). Absolute paleointensity study of Miocene Tiva Canyon Tuff, Yucca Mountain, Nevada: role of fine-particle grain-size variations. *Geochemistry, Geophysics, Geosystems*, *20*, 5818–5830. https://doi.org/10.1029/2019GC008728

Received 19 SEP 2019
Accepted 15 NOV 2019
Accepted article online 19 NOV 2019
Published online 04 DEC 2019

Absolute Paleointensity Study of Miocene Tiva Canyon Tuff, Yucca Mountain, Nevada: Role of Fine-Particle Grain-Size Variations

F. Abdulghafur[1] and **J. A. Bowles**[1]

[1]Department of Geosciences, University of Wisconsin-Milwaukee, Milwaukee, WI, USA

Abstract Fine-grained, Ti-poor titanomagnetite in the ~12.7 Ma Tiva Canyon (TC) Tuff systematically increases in grain size from superparamagnetic (SP) at the flow base to single domain (SD) at a few meters height. This allows us to examine the role of grain-size variation on paleointensity, within the transition from SP to stable SD. We present magnetic properties from two previously unreported sections of the TC Tuff, as well as Thellier-type paleointensity estimates from the lowermost ~7.0 m of the flow. Magnetic hysteresis, frequency-dependent susceptibility, and thermomagnetic data show that sample grain-size distribution is dominated by SP in the lower ~3.6 m, transitioning upwards to mostly stable SD. Paleointensity results are closely tied to stratigraphic height and to magnetic properties linked to domain state. SD samples have consistent absolute paleointensity values of 28.5 ± 1.94 μT (VADM of 51.3 ZAm^2) and behaved ideally during paleointensity experiments. The samples including a significant SP fraction have consistently higher paleointensities and less ideal behavior but would likely pass many traditional quality-control tests. We interpret the SD remanence to be a primary thermal remanent magnetization but discuss the possibility of a partial thermal-chemical remanent magnetization if microcrystal growth continued at $T < T_c$ and/or the section is affected by post-emplacement vapor-phase alteration. The link between paleointensity and domain state is stronger than correlations with water content or other evidence of alteration and suggests that the presence of a significant SP population may adversely impact paleointensity results, even in the presence of a stable SD fraction.

Plain Language Summary The strength—or intensity—of Earth's magnetic field changes over geologic time, and these changes are important in learning about the internal evolution and processes of Earth's core. These "paleointensity" variations are recorded in many Earth materials, including volcanic ash flows, sometimes called "tuffs." Magnetic minerals in these flows acquire a magnetization proportional to Earth's field strength when they cool. The approximately 12 million-year-old Tiva Canyon Tuff in the western United States contains very fine-grained magnetite particles, the size of which increases upwards from the base of the flow. This small size is typically considered ideal for a paleointensity recorder, and the systematic size variation allows us to test effect of grain size on the paleointensity estimation across the lower end of the size spectrum. Samples collected from the lowermost 7 m of the Tiva Canyon Tuff were subjected to laboratory experiments designed to recover paleointensity. We find that the smallest particles perform poorly in the experiments and do not produce consistent results, while the slightly larger particles perform ideally and provide a consistent answer. This tells us that smaller is not always better, and there is a very narrow grain size range that will produce accurate results.

1. Introduction

Absolute geomagnetic paleointensity estimates play an important role in our understanding of geodynamo processes. Most absolute paleointensity methods require samples that carry noninteracting single domain (SD) size particles, but such ideal SD grains are rarely found in nature. One rare example of true SD-sized natural particles is found in the middle Miocene (~12.7 Ma) Tiva Canyon (TC) Tuff of Yucca Mountain, Nevada. Previous work has established that primary magnetic remanence carriers in the basal vitric zone of the TC Tuff are needle-shaped, low-Ti magnetite microcrystals that vary systematically from superparamagnetic (SP) near the base of the unit upwards into single domain/pseudo-single domain (SD/PSD) as a result of natural variations in cooling rates in the pyroclastic ash flow (Jackson et al., 2006; Rosenbaum, 1986, 1993; Schlinger et al., 1988, 1991; Till et al., 2011; Worm & Jackson, 1999). It is inferred that the Ti-poor titanomagnetite precipitated out of the glass matrix at elevated temperatures $T > 500$ °C (Schlinger et al.,

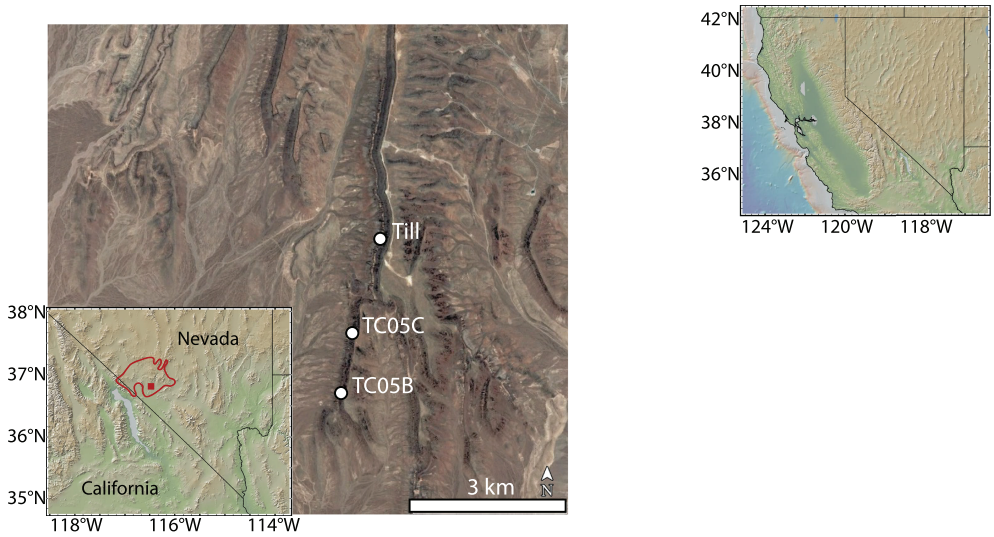

Figure 1. Sample location map. Sample locations shown by white dots, along with location of Till et al. (2011) data. Imagery from GoogleEarth. Inset shows regional location of study area. Thin red line is extent of Tiva Canyon Tuff (from Warren et al., 1989). Small red square is location of this study area.

1988, 1991). The TC Tuff provides an excellent opportunity to evaluate paleointensity performance as a function of grain size.

The rock magnetic properties of the TC Tuff are documented by abundant published data (Egli & Lowrie, 2002; Jackson et al., 2006; Rosenbaum, 1986, 1993; Rosenbaum & Rivers, 1984; Rosenbaum & Snyder, 1984; Schlinger et al., 1988, 1991; Till et al., 2011; Worm & Jackson, 1999), and the geologic setting of the TC Tuff has been extensively studied due to its proximity to the potential nuclear waste repository at Yucca Mountain (Buesch et al., 1996; Flint et al., 2001; Frizzell & Shulters, 1990; Gibson et al., 1992; Istok et al., 1994; Levy et al., 1995; Moyer et al., 1997; Rautman & Engstrom, 1996). In this paper, we present the first paleointensity results from the basal vitric zone TC Tuff, as well as previously unpublished rock magnetic results from two new sections.

2. Geologic Background

The TC Tuff is exposed on the west flank of Yucca Mountain (Figure 1), in the central the part of the Southwest Nevada Volcanic Field (SWNVF). The SWNVF was active between 7.5 and 15 Ma and is composed of more than six calderas and numerous magmatic deposits with estimated volumes of more than 10,000 km^3 (Lipman, 1966; Byers et al., 1976, 1989; Sawyer et al., 1994; Buesch et al., 1996; Rautman & Engstrom, 1996). Between 14.0 and 11.4 Ma, volumetric pyroclastic flows and their associated fallout tephra deposits were erupted from Yucca Mountain (Byers et al., 1989; Sawyer et al., 1994). The Yucca Mountain rock units are divided into the lower Crater Flat Group and the upper Paintbrush Group. The Paintbrush Group is further subdivided into the lower Topopah Spring Tuff Formation (12.8 Ma, ~1,200 km^3) and the upper TC Tuff Formation (>1,000 km^3) (Byers et al., 1976, 1989; Rautman & Engstrom, 1996; Sawyer et al., 1994). Originated from the Claim Canyon Caldera (Byers et al., 1976; Rautman & Engstrom, 1996; Sawyer et al., 1994), the 12.7 ± 0.03 Ma TC Tuff ($^{40}Ar/^{39}Ar$ dates by Sawyer et al., 1994) is a rapidly emplaced multiple-flow compound cooling unit that is compositionally zoned from a crystal-poor (<7–10%) rhyolite base (77% SiO_2) to a crystal-rich (>7–10%) quartz latite top (69% SiO_2) (Lipman, 1966; Byers et al., 1976; Rosenbaum, 1986; Buesch et al., 1996). The TC Tuff varies in thickness up to 200 m (Lipman, 1966; Byers et al., 1976; Busech et al., 1996; Rautman & Engstrom, 1996; Keefer et al., 2007).

The roughly 15-m crystal-poor vitric basal zone (Tpcpv) of the TC Tuff has been subdivided into three subzones from the base to the flow interior (Buesch et al., 1996): a 2–9 m thick non-welded basal subzone (Tpcpv1), a 1–5 m thick moderately welded middle subzone (Tpcpv2), and a 0–3 m thick densely welded upper subzone (Tpcpv3). The Tpcpv1 has undeformed pumice clasts in a matrix that is vitric to weakly

vapor-phase altered. The Tpcpv2 has partially deformed pumice clasts in a matrix that is locally vapor-phase altered. The Tpcpv3 is exposed locally on the flank of Yucca Mountain in Solitario Canyon. Our samples were collected from the lower ~7 m within Tpcpv and contain some lithic fragments as well as pumice lapilli.

2.1. Emplacement and Post-Emplacement Conditions

Two questions should be asked in regard to the origin of the remanent magnetization in the samples. First, is the magnetomineralogy formed at elevated temperatures ($T > T_c$) and thus the remanence is a total thermoremanent magnetization (TRM)? Second, is there any secondary alteration in the samples that may affect remanence?

The remanence-carrying titanomagnetites in the sampled Tpcpv layer of the TC Tuff are inferred to have formed by precipitation from volcanic glass at elevated temperatures during or immediately after the flow emplacement (Rosenbaum, 1993; Schlinger et al., 1988, 1991). Estimated emplacement temperatures for the TC Tuff were inferred to be between 660 and 900 °C, based on mineral equilibration temperature calculations (e.g., Lipman, 1966; Warren et al., 1989). The nature of the remanence therefore depends on whether or not post-emplacement grain growth ceased at $T > T_c$. Grain growth is assumed to cease below the glass transition temperature (T_g), the temperature at which glass transitions from liquid-like to solid-like behavior. T_g has also been taken to represent the minimum welding temperature in the silicic Gray's Landing ignimbrite basal vitrophyre, where T_g was measured at 870 °C (Lavallée et al., 2015). Lower estimates (~550–600 °C) for minimum welding temperature typically relate to the flow interior where high pressure and slow cooling lead to an extended welding window (e.g., Grunder et al., 2005; Riehle, 1973; Sheridan & Ragan, 1975). In the basal vitrophyre, however, cooling is rapid, and welding is expected to cease at higher temperatures. Although T_g data for the TC Tuff vitrophyre do not exist, typical T_g of fresh, low-H_2O, natural glasses is ~650–800 °C (Giordano et al., 2005). However, the addition of 1-2 wt% water will dramatically reduce T_g to ~500–600 °C (Giordano et al., 2005).

The nature of the remanence also depends on whether or not the magnetic particles were chemically altered during or after cooling. Alteration may take place during devitrification of the flow, high-temperature vapor-phase alteration, and/or interaction with water at lower temperatures. Early research found that the vitric basal zone of the TC Tuff is unaltered (Sykes et al., 1979), as pristine rhyolitic and dacitic glass were observed with little evidence of devitrification, filled fractures, vapor-phase alteration, or zeolitization. Sykes et al. (1979) observed weakly vapor-phase altered pumice clasts and weakly devitrified materials between glass shards in Tpcpv. Busech et al. (1996) reported a Tpcpv1 subzone that has weakly vapor-phase altered matrix and pumice clasts that are either glassy or replaced partially or wholly by vapor-phase minerals. Tpcpv2 is characterized by a moderately welded, locally vapor-phase altered matrix with partially deformed pumice clasts. These clasts may be vitric, devitrified, or replaced by vapor-phase minerals. A low degree of fracturing and no significant free water were observed within the Tpcpv zone (Buesch et al., 1996). The presence of smectite and the absence of illite in the Tpcpv and is interpreted to potentially result from currently forming low-temperature alteration of the glass (Chipera et al., 1995).

The basal Tpcpv zone is far less altered than the devitrified flow interior (Buesch et al., 1996; Rautman & Engstrom, 1996), but it is conceivable that thermochemical remanent magnetization (TCRM) may have formed at least locally and would adversely impact paleointensity results. We therefore measure the water content of our samples to assess the amount of possible (re)hydration.

3. Magnetic Mineralogy and Rock Magnetic Background

The magnetic remanence carrier in the Tpcpv is low-Ti titanomagnetite, and grain size systematically increases upsection (Jackson et al., 2006; Rosenbaum, 1986, 1993; Schlinger et al., 1988, 1991; Till et al., 2011; Worm & Jackson, 1999). The magnetocrystals' grain-size variations have been interpreted to arise from natural variations in cooling rate (Lipman, 1971; Schlinger et al., 1988, 1991).

Many studies (Egli & Lowrie, 2002; Jackson et al., 2006; Rosenbaum, 1986, 1993; Schlinger et al., 1988, 1991; Till et al., 2011; Worm & Jackson, 1999) have documented rock magnetic properties within the Tpcpv zone that are linked to the observed grain-size variations. In the most thorough rock magnetic study, Till et al. (2011) measured bulk magnetic susceptibility (χ_0), susceptibility of anhysteretic remanent magnetization (χ_{ARM}), low-temperature ($T < 400$ K) alternating current (AC) susceptibility, saturation remanent

magnetization (M_{rs}), saturation magnetization (M_s), coercivity (B_c), and coercivity of remanence (B_{cr}) in a 5 m interval of the Tpcpv zone (Figure 1; sample location-IV from Schlinger 1991). They interpreted their data in terms of grain-size variation and magnetic domain state, such that SP behavior dominates at the base of the flow (<0.8 m) and transitions to SD behavior within a few meters (3.25 m). Maxima in χ_{ARM}, M_{rs}/M_s, and B_c are interpreted to represent the upper limit of stable SD behavior at 3.25 m above the base. Above this level, decreases in M_{rs}/M_s and B_c suggest a transition from SD to PSD behavior.

Transmission electron microscopy observations document needle-shaped grains that increase in size from ~5 × 15 nm near the base to ~50 × 500 nm at 2.6 m above the base (Schlinger et al., 1991). Semiquantitative X-ray analysis documented a composition of Fe (2.7–2.95), Ti (0–0.03), Cr (0–0.18), and Mn (0–0.24) per formula unit with T_c ~540 °C (Schlinger et al., 1991).

Alternating field (AF) and thermal demagnetization of TC Tuff samples showed a single stable direction of magnetization that is reversely magnetized with a tilt-corrected mean direction of D = 181.0°, I = −42.4° (Rosenbaum et al., 1991), consistent with eruption during chron C5Ar.2r (Gee & Kent, 2007).

4. Methods

4.1. Field Methods

Unoriented, 1″ diameter cores were collected from the lower ~7 m within the Tpcpv zone with a gas-powered drill from two sections of the TC Tuff site TC05B (36.79193°N, 116.47887°W) and TC05C (36.80378°N, 116.47640°W), near the Rosenbaum (1986, 1991), Schlinger et al. (1991), and Till et al. (2011) sampling locations (Figure 1). Cores were subdivided into ~1 inch long specimens.

4.2. Loss On Ignition and Density

We measured loss on ignition (LOI) on six specimens as a means of assessing possible rehydration which may be linked to secondary alteration. The specimens were selected at ~ 2 m depth intervals, four from section TC05B and two from section TC05C. Approximately 1 g of each specimen was powdered and kept in the oven at 120 °C overnight to drive off excess surface moisture. The empty ceramic crucible was placed into a furnace at 1050 °C for 6–8 min and cooled in a desiccator for 5 min. Next, the original weight of the crucible and the powdered specimen were measured separately with 1 μg precision. The specimen was then placed in the crucible and kept in the furnace for 15 min at 1050 °C and removed to the desiccator to cool for 10 min. Then the specimen and crucible weight were taken together, and LOI was calculated as the percentage weight loss and is assumed to be the total volatile content.

Specimen density was calculated by measuring the dimensions and mass of the cores.

4.3. Rock Magnetic Measurements

Hysteresis loops were measured on a Princeton Measurements MicroMag Vibrating Sample Magnetometer (VSM) or a Princeton Applied Research VSM. Magnetization was measured as a function of applied field up to ±1 T, and data were processed as in Jackson and Solheid (2010). Room temperature susceptibility was measured as a function of frequency from 109 to 9901 Hz (TC05B) and from 920 to 5002 Hz (TC05C) on a MAGNON Variable Frequency Susceptibility Meter. Frequency-dependent susceptibility (χ_{fd}) was calculated as $\chi_{fd} = 100\,[\chi(f_1) - \chi(f_2)]/\chi(f_1)/\log_{10}(f_2/f_1)$, where f_1 = 109 Hz and f_2 = 9901 Hz for TC05B and f_1 = 920 Hz and f_2 = 5002 Hz for TC05C. All measurements were made at the Institute for Rock Magnetism, University of Minnesota. Additional temperature-dependent susceptibility, χ(T), measurements were made at University of Wisconsin-Milwaukee (UWM) on an AGICO MFK1-FA MultiFunction Kappabridge with CS4 furnace attachment under flowing Ar. Most measured specimens were previously heated as part of the paleointensity experiments (section 5.3), but results showed no systematic differences between samples that had and had not been previously heated.

4.4. Paleointensity Experiments

Thirty-three specimens were subjected to paleointensity analysis using the IZZI variation (Tauxe & Staudigel, 2004) of the Thellier and Thellier (1959) method. In the IZZI protocol, the order of the in-field and zero-field steps is reversed at each temperature step. To assess laboratory alteration, partial TRM (pTRM) checks (Coe et al., 1978) were used at every other temperature step. Samples were heated in

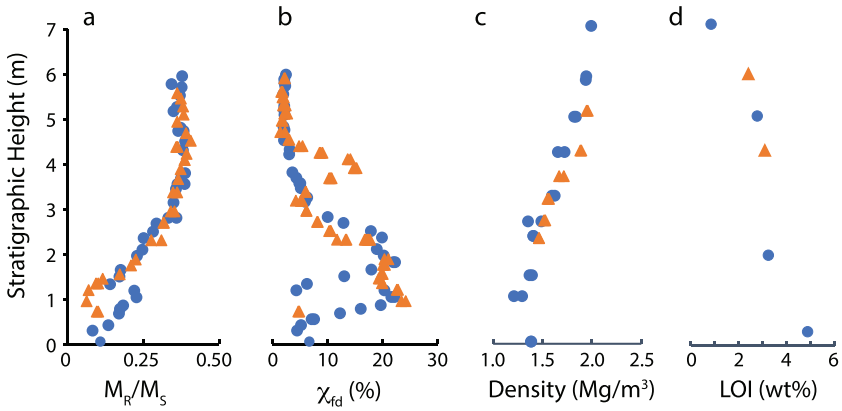

Figure 2. Rock magnetic and physical property measurements from the TC05 samples with stratigraphic height. (a) M_R/M_S; (b) frequency-dependent susceptibility, χfd (%); (c) density (Mg/m^3); and (d) loss on ignition (LOI, wt%), an estimate of water content. Blue circles are section TC05B; orange triangles are section TC05C. Magnetic properties are consistent with an upsection increase in magnetic grain size from SP to SD, while density and LOI show an increase in degree of welding and decrease in water content, respectively.

nitrogen atmosphere, and a field of 40 μT was applied during the in-field heating and cooling steps. Heating increments were 50 °C from 100 to 400 °C; 25 °C from 400 to 500 °C; and 15 °C from 500 to 590 °C. Experiments were conducted inside the shielded room at the UWM Paleomagnetic Laboratory using an ASC TD-48SC furnace. Remanence was measured on a Molspin Minispin magnetometer using a 6-position measurement scheme. Room temperature susceptibility was measured on a Bartington MS2B susceptibility bridge.

Because it has been demonstrated that TRM acquisition may be nonlinear in magnetic minerals with large aspect ratios (Selkin et al., 2007), we evaluate the linearity of our samples by acquiring a total TRM from 600 °C in fields of 10, 20, 40, and 60 μT.

A cooling rate correction was calculated using a cooling model where the boundary condition at the base of the flow is allowed to evolve as the country rock heats up via conduction (Turcotte & Schubert, 2002). For simplicity, the top and bottom of the flow were treated the same, although the boundary conditions would be different at the top of the flow. Because of the thickness of the flow (200 m), this does not affect the calculations at the base over the temperature intervals of interest. Estimated pre-eruptive magmatic temperatures for the TC Tuff range from 660 to 900 °C (e.g., Flood, 1987; Lipman, 1966; Warren et al., 1989). Assuming a rapid eruptive mechanism, we take 800 °C as an approximation for emplacement temperature. We also use an average flow thickness of 200 m (Byers et al., 1976; Rautman & Engstrom, 1996), a starting boundary condition of 25 °C, a thermal conductivity of 1.5 Wm^{-1} K^{-1}, and a thermal capacitance of 2.2 J cm^{-3} K^{-1} (Brodsky et al., 1997). Thermal properties of the flow and the country rock are assumed to be the same. The laboratory cooling rate is ~1.70 °C/h at 580 °C, and paleointensity is assumed to be overestimated by 5% for each order of magnitude decrease in natural cooling rate (Fox & Aitken, 1980; Halgedahl et al., 1980).

5. Results

5.1. LOI and Density Results

For both sections, density increases with increasing profile height from ~1.2 to ~2.0 Mg/m^3 (Figure 2c). The LOI value decreases with increased profile height (Figure 2d), where the lowermost Tpcpv specimen TC05B-3c (0.3 m) has the highest value (4.88 wt%) and the uppermost Tpcpv specimen TC05B-43-2c (6.96 m) shows the lowest LOI (0.85 wt%).

5.2. Rock Magnetic Results

Our rock magnetic results are consistent with increasing magnetic grain size with stratigraphic height in both sections (Figures 2a and 2b). Samples near the base of the flow tend to have hysteresis loops with very little remanence (Figure 3a), consistent with SP grains. Moving upsection, loops become more open and

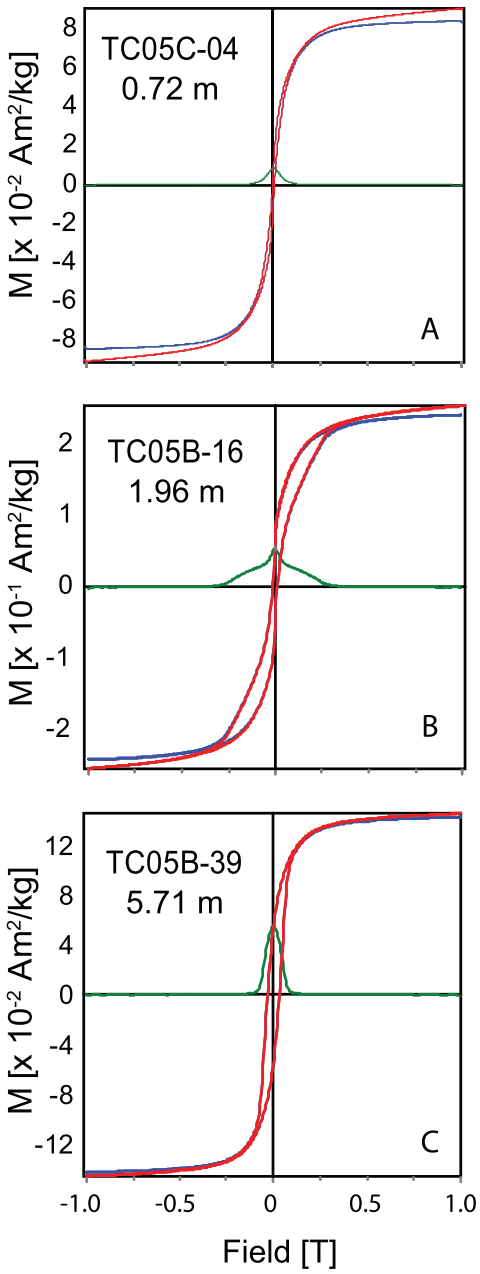

Figure 3. Example hysteresis loops. Many samples near the base of the flow have closed loops with little-to-no remanence, characteristic of SP grains (a). Samples from higher up show predominantly SD behavior (c). At site (b) only, loops between ~0.6 and 5 m are wasp-waisted and close at relatively high field values. Red curves are raw data. Blue curves are corrected for paramagnetic behavior. Green curves are M_{rh}.

show predominantly SD behavior (Figure 3c). At site B only, samples between approximately 0.6 and 5 m display variable degrees of wasp-waistedness (Figure 3b) indicating a mixture of two phases with different coercivities. These loops also close at anomalously high field values (up to ~450 mT), as shown by M_{rh} in green in Figure 3 (M_{rh} = [upper branch of loop − lower branch of loop]/2; e.g., Jackson & Solheid, 2010). This suggests the presence of a higher coerceivity phase, such as (titano)hematite. To our knowledge, no hematite has been documented in the base of the flow, but it has been observed in places in the upper, devitrified parts of the flow (Chipera et al., 1995).

The ratio of M_r to M_s increases from ~0.08 at the base to ~0.35–0.4 at 3.0 m and then remains relatively constant between 3.0 and 6.0 m. While samples from TC05C increase nearly monotonically from the base to 3.0 m, TC05B displays a local maximum at ~1 m. This overall trend is characteristic of SP grains that have little-to-no remanence at the base, increasing in size to stable SD.

Frequency-dependent room temperature susceptibility (χ_{fd}) in both sets increases from ~4% at the base to ~20% at ~1 m. Above ~3 m χ_{fd} decreases to near constant values of ~2.5%. Notable exceptions to this pattern are lower values in TC05B near 1.5 m and higher values in TC05C near 4 m that may be related to individual pulses of the eruption.

The variations in χ_{fd} are interpreted to reflect the thermally activated blocking process and represent the fraction of grains that have blocking temperatures close to room temperature (Thompson & Oldfield, 1986). Thus, the finest SP grains at the base of the flow have blocking temperatures well below room temperature and χ_{fd} is low. χ_{fd} increases to a peak where blocking temperatures are close to room temperature and then decreases with height as grain size and blocking temperature increase. This trend corresponds with an increase in NRM unblocking temperatures observed during the paleointensity experiments, and the overall rock magnetic trends are very similar to those observed by Till et al. (2011).

Thermomagnetic data also reveal the increase in blocking temperatures with height (Figure 4). Most samples were reversible on cooling and display a peak in susceptibility that we interpret to be associated with the thermally activated blocking. This peak shifts to increasingly higher temperatures with stratigraphic height. For samples at heights > ~3.25 m, there is an indication of two Curie temperatures (~470 and ~560 °C), which may be linked to slightly different grain size or compositional populations.

5.3. Paleointensity Results

Paleointensity results of selected specimens are tabulated in Table 1 and illustrated in Figure 5 which shows the range of behaviors observed. The temperature steps included in the data interpretation are chosen to avoid any low-temperature viscous overprint and to have a consistent temperature range for the selected specimens. All specimens from the SD range Tpcpv zone (≥ 3.24 m) display univectoral decay of the NRM, after the removal of a viscous component by 300–350 °C in most of the samples (Figures 6e–6i). Specimens from <3.24 m tend to have Arai plots that deviate from linearity, especially at low temperatures (Figures 6a–6d). These specimens also typically have a larger overprint that is roughly antiparallel to the main component (e.g., Figure 6d), have a higher degree of scatter in the Arai plots, as documented by the standard error of the slope, σ_b (Coe et al., 1978; Figure 5d), and have steeper slopes. There is an irregular data point in

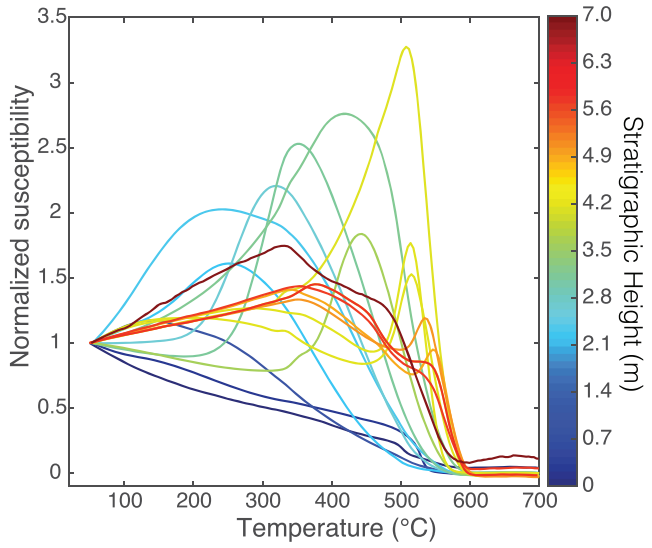

Figure 4. Thermomagnetic results. Only heating curves are shown; most data were reversible on cooling. Peak in susceptibility linked to blocking temperature and increases with increasing stratigraphic height.

Figure 6f, which is excluded from the Arai plot. Two specimens from 0.05 m show MD-like concave-up Arai plot behavior (Figure 6a).

Samples from the lower part of section B (<3.2 m) have a significant fraction of the remanence (~20%) remaining at T > 590 °C (e.g., Figures 5b and 5c). This coincides with the most wasp-waisted loops (section 5.2) and is consistent with some fraction of the remanence held by titanohematite. Compared to the same stratigraphic interval at section C, however, there are no significant differences in paleointensity behavior or slope. The presence of the high-coercivity phase does not therefore appear to influence the paleointensity results.

f, the NRM fraction used in the paleointensity calculation (Figure 5b) (Coe et al., 1978), decreases with height up to ~3.24 m, then increases, and shows stable values close to 1. There is an increase in the quality factor, *q*, (Coe et al., 1978) (Figure 5c), which starts as low as 4.6 in the lower Tpcpv and reaches as high as 62.3 at 4.23 m. σ_b (Figure 5d) decreases with increasing stratigraphic height from 0.1 to 0.054 at 3.17 m; from this height, it reaches a stable range between 0.013 and 0.017. DRAT, the percentage ratio which defines the difference between repeat pTRM steps divided by the length of the selected NRM-pTRM segment (Selkin & Tauxe, 2000) (5e), is mostly constant at about 0.7–4.2, with the exception of TC05C samples between ~2 and 4 m where values are up to 19.6. The stratigraphic changes in most of these values are not gradual but rather undergo a step change at ~3.25 m from lower-quality results below to higher-quality results above.

Lower Tpcpv zone specimens from both sections show rather high and inconsistent paleointensity results, ranging from 35.6 to 77.5 μT after the cooling rate correction is applied. By contrast, Tpcpv specimens ≥3.24 m have more stable and consistent values (Figure 6, Table 1), ranging from 25.2 to 31.5 μT.

For the final paleointensity interpretation in this study, we select the specimens which have stable SD rock magnetic behavior. These specimens also have the lowest LOI and high quality-control statistics, so we do not additionally apply any specific threshold criteria. These specimens have an internally consistent paleointensity value, and we consider them to be the best representation of the true field value. Nine and eight specimens are selected from TC05B and TC05C sections, respectively. A final average cooling rate corrected paleointensity value calculated from 17 SD specimens is 28.5 ± 1.94 μT.

The linearity test revealed a linear trend in TRM acquisition in all the selected specimens with increasing laboratory fields (supporting information Figure S1) except for three specimens from the stratigraphic heights >5.88 m. They showed a deviation at 40 μT and then merged back to the standard normalized magnetization. Further, there is no evidence for remanence anisotropy based on the small angle between the final TRM and the applied field (average of 2.2°; Figure S2).

6. Discussion

As noted in the results section, the Tpcpv zone specimens ≥3.24 m display internally consistent paleointensity results (mean 28.5 μT), which are apparently linked to the more slowly cooled, needle-shaped, well-separated, noninteracting SD domain state of the iron-oxide microcrystals with high unblocking temperatures. The majority of specimens from this zone show ideal linear behavior in the NRM-pTRM plots with DRAT ≤4.2% with the exception of 19.6% at 3.67 m.

By contrast, the samples from lower Tpcpv (<3.24 m) have higher paleointensities (>35.6 μT) derived from lower-quality data and are characterized by a smaller magnetic grain size and lower average unblocking temperatures. Figure S3 shows unblocking variations with stratigraphic height. Schlinger et al. (1988) point out that the SP grains of the TC Tuff will carry a soft remanence and will be easily influenced by the recent magnetic field. When the samples were collected in 2005, the field strength at Yucca Mountain was 49.9 μT, and global field strength has been declining for at least several hundred years (e.g., Korte & Constable, 2011). After collection, samples were stored in Minneapolis, Minnesota, where the field strength is ~55 μT. While

Geochemistry, Geophysics, Geosystems

10.1029/2019GC008728

Table 1
Tiva Canyon Tuff Specimen Level Paleointensity Results

Sample	H (m)	B_{anc}	% cor	$B_{anc\text{-}cor}$	err	N_{pts}	T_{Lo}	T_{Hi}	f	g	σ_b	σ_b/b	q	NRM	MAD	DANG	DRAT	f_{VDS}	N_{pTRM}
TC05B-1c	0.05	18.5	5.69	16.8	2.12	14	200	590	1.069	0.894	0.053	0.115	8.3	1.92E-03	6.6	2.7	3.1	0.684	14
TC05B-1d	0.05	17.8	5.69	17.5	2.24	14	200	590	1.124	0.888	0.056	0.125	8.0	1.74E-03	4.0	2.7	2.0	0.806	14
TC05B-9c	1.04	82.3	6.21	77.5	5.68	13	300	590	0.524	0.871	0.142	0.069	6.7	5.76E-03	5.3	1.6	4.6	0.563	13
TC05B-9d	1.04	74.2	6.21	69.9	6.52	13	300	590	0.562	0.821	0.163	0.088	5.6	5.36E-03	2.9	0.7	5.3	0.607	13
TC05B-13-2c	1.50	41.0	6.27	38.6	3.72	13	300	590	0.663	0.812	0.093	0.090	6.0	3.15E-03	6.8	3.0	3.9	0.487	13
TC05B-13-2d	1.50	42.9	6.27	40.4	4.00	13	300	590	0.661	0.877	0.100	0.093	5.8	3.52E-03	6.2	2.1	4.6	0.504	13
TC05B-18-2b	2.36	65.7	8.99	60.3	5.92	13	300	590	0.419	0.887	0.148	0.090	4.1	7.36E-03	4.6	1.8	9.5	0.532	13
TC05B-18-2c	2.36	63.2	8.99	58.0	4.64	13	300	590	0.399	0.862	0.116	0.074	4.8	7.13E-03	8.2	3.1	7.5	0.486	13
TC05B-20-2b	2.68	45.8	9.64	41.8	3.84	13	300	590	0.399	0.865	0.096	0.084	4.1	7.63E-03	5.1	3.5	11.2	0.486	13
TC05B-20-2c	2.68	44.7	9.64	40.8	3.24	13	300	590	0.418	0.863	0.081	0.072	5.0	7.39E-03	5.5	4.9	10.1	0.516	13
TC05B-23-2b	3.24	31.9	10.56	28.9	0.76	13	300	590	0.541	0.860	0.019	0.024	19.3	1.27E-02	2.8	3.0	2.0	0.525	13
TC05B-23-2c	3.24	32.2	10.56	29.1	0.84	13	300	590	0.527	0.864	0.021	0.027	17.1	1.18E-02	3.5	4.1	4.2	0.532	13
TC05B-28-2b	4.20	30.1	11.78	26.9	1.12	11	400	590	0.726	0.868	0.028	0.038	16.7	2.50E-02	3.8	3.3	3.0	0.612	11
TC05B-28-2c	4.20	28.2	11.78	25.2	0.68	12	350	590	0.840	0.830	0.017	0.024	30.2	2.74E-02	2.1	0.5	2.4	0.735	12
TC05B-34-1b	4.97	29.9	12.55	26.6	0.48	12	350	590	0.909	0.830	0.012	0.016	47.8	5.96E-02	4.0	0.5	2.2	0.646	12
TC05B-34-1c	4.97	30.1	12.55	26.7	0.44	12	350	590	0.902	0.813	0.011	0.015	50.8	5.94E-02	4.8	0.5	4.2	0.652	12
TC05B-40-1c	5.78	35.2	13.24	31.1	0.56	12	350	590	0.940	0.810	0.014	0.016	47.6	9.68E-02	3.9	0.5	1.6	0.678	12
TC05B-41-1c	5.86	35.4	13.30	31.2	0.72	12	350	590	0.934	0.897	0.018	0.020	37.9	8.59E-02	3.2	0.5	2.9	0.702	12
TC05B-43-2b	6.96	32.7	14.07	28.7	1.00	12	350	590	0.781	0.888	0.025	0.030	23.2	6.09E-03	2.8	0.3	2.4	0.692	12
TC05C-13-1c	2.31	49.7	8.88	45.6	4.84	13	300	590	0.348	0.850	0.121	0.097	3.0	4.39E-03	4.1	1.5	13.5	0.405	13
TC05C-13-1d	2.31	49.2	8.88	45.2	4.52	13	300	590	0.341	0.857	0.113	0.092	3.2	4.25E-03	2.4	1.1	12.9	0.419	13
TC05C-16-2b	2.70	49.2	9.67	44.9	6.20	13	300	590	0.199	0.816	0.155	0.126	1.3	4.66E-03	3.9	2.3	14.8	0.298	13
TC05C-16-3b	2.70	52.8	9.67	48.1	5.56	13	300	590	0.197	0.840	0.139	0.106	1.6	4.34E-03	4.2	1.3	11.1	0.295	13
TC05C-18-1c	3.17	46.2	10.46	41.8	4.68	13	300	590	0.302	0.823	0.117	0.101	2.5	7.63E-03	4.8	3.7	17.8	0.386	13
TC05C-18-1d	3.17	39.3	10.46	35.6	4.16	12	350	590	0.193	0.843	0.104	0.105	1.5	4.12E-03	5.8	2.3	5.7	0.212	12
TC05C-20-1c	3.67	35.0	11.15	31.5	1.20	13	300	590	0.692	0.852	0.03	0.035	17.1	1.72E-02	2.7	2.5	19.6	0.664	13
TC05C-20-1d	3.67	34.5	11.15	31.0	1.20	13	300	590	0.693	0.843	0.03	0.034	17.0	1.88E-02	1.9	2.1	19.4	0.665	13
TC05C-23-1c	4.23	32.9	11.81	29.4	0.64	12	350	590	0.949	0.828	0.016	0.019	41.6	3.76E-02	1.6	0.3	0.7	0.81	12
TC05C-23-1d	4.23	33.4	11.81	29.9	0.44	12	350	590	0.952	0.83	0.011	0.012	62.3	3.71E-02	2.3	0.5	1.3	0.737	12
TC05C-28-1c	5.10	31.6	12.67	28.0	0.64	12	350	590	0.939	0.827	0.016	0.020	39.3	6.24E-02	3.0	0.3	1.9	0.648	12
TC05C-28-1d	5.10	31.3	12.67	27.8	0.60	12	350	590	0.95	0.829	0.015	0.020	40.2	6.82E-02	2.1	0.4	1.3	0.765	12
TC05C-32-2c	5.88	29.8	13.32	26.3	0.44	12	350	590	0.946	0.773	0.011	0.015	48.4	8.39E-02	3.7	0.6	2.6	0.713	12
TC05C-32-2d	5.88	29.6	13.32	26.1	0.44	12	350	590	0.964	0.778	0.011	0.015	49.4	7.87E-02	2.5	0.6	1.7	0.613	12

Note. Laboratory field of 40 μT is used for all specimens. %cor. = % cooling rate correction applied; σ_b = standard error of the slope; σ_b/b = best fit slope; B_{anc} = ancient field (μT); $B_{anc\text{-}cor}$ = cooling rate corrected ancient field (μT); DANG = deviation angle between the vector average of the selected data with the principal component; DRAT = difference ratio defined as the difference between repeat pTRM steps, normalized by the length of the selected the NRM-pTRM segment, expressed as a percentage; err = standard error of the slope multiplied by the Blab (Coe et al., 1978); f = NRM fraction; f_{VDS} = NRM fraction based on vector difference sum; g = gap factor; H = specimen height (m); MAD = maximum angular deviation (Kirschvink, 1980); N_{pTRM} = number of pTRM checks included in analysis (Selkin & Tauxe, 2000); N_{pts} = number of temperature steps included in analysis;
NRM = natural remanent magnetization (Am^2/kg); q = quality factor (Coe et al., 1978); T_{lo}, T_{hi} = minimum and maximum temperature steps included in analysis (°C).

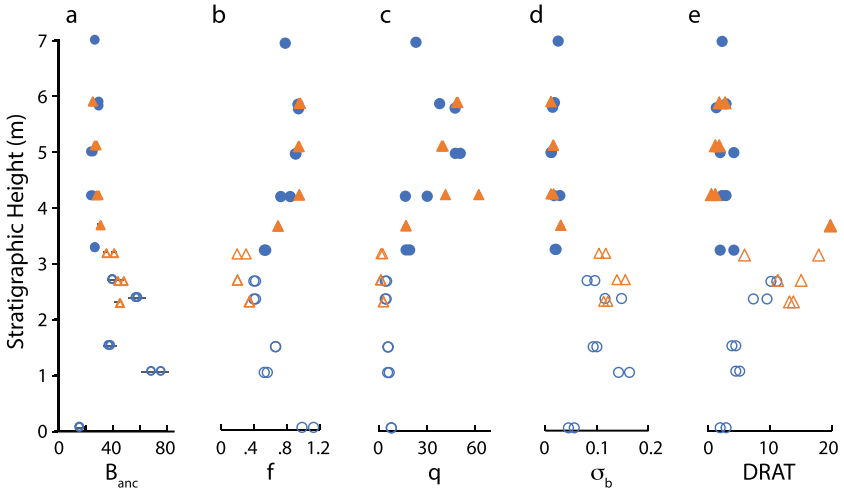

Figure 5. Paleointensity results and statistics. Closed circles (TC05B) and triangles (TC05C) are specimens included in the final paleointensity estimate. Open symbols were excluded. (a) Paleointensity interpretation, B_{anc}. Error bars represent sb*Blab, and some are smaller than symbol size. (b) NRM fraction, (f, c) quality factor, *q*; and (d) standard error of the slope, sb (Coe et al., 1978). (e) Difference ratio, DRAT (Selkin & Tauxe, 2000).

the low unblocking temperatures of the finest grains lend themselves to viscous overprinting over thousands or millions of years, unblocking in all samples extends to well over 300 °C. These grains should be stable at ambient temperatures for billions of years (e.g., Pullaiah et al., 1975), and standard Néel theory therefore does not fully explain the steep slopes and high paleofields found in these samples.

Another material that has a range of fine grain sizes spanning the SP-SD range is basaltic glass. Bowles et al. (2011) published paleointensity results on a set of synthetic basaltic glasses created under controlled conditions. In that work, specimens that did not meet stringent paleointensity quality-control criteria were excluded from analysis. Many of the excluded specimens were the most weakly magnetic and least crystalline samples, containing the smallest grain-size population. Including these specimens, however, we find that for specimens with NRMs greater than about 3.5×10^{-4} Am^2/kg, the recovered paleointensity is within 20% of the actual value (Figure S4). For specimens with weaker NRMs, recovered paleointensities vary between −40% and +70% (with two specimens > +100%). While this is not exactly analogous to the Tiva Canyon findings where the more SP samples always produce higher paleointensities, it reinforces the idea that a grain-size distribution that includes a significant SP fraction results in nonideal behavior.

Finally, we point out that the MD-like behavior and the unusually low paleointensity value (16.0 μT) at the base of the Tpcpv (0.05 m) perhaps is caused by incorporation of pre-TC materials into the base of the flow.

6.1. Possible Effects of (Re)hydration and/or TCRM on Paleointensity

While there appears to be a clear link between domain state and paleointensity results, we consider whether or not some form secondary alteration may affect the paleointensity estimates via acquisition of a TCRM or CRM. High LOI values in our samples are associated with higher paleointensity estimates of somewhat lower quality, suggesting there may be a link to secondary alteration. In the Bishop Tuff, Avery et al. (2018) find higher paleointensity associated with vapor-phase alteration, the added presence of titanohematite, and a TCRM. An opposite trend is observed by Bowles et al. (2015) who reported less reliable and lower paleointensity results from the 1912 Novarupta ash flow tuffs containing >0.75 wt% water. Ferk et al. (2011, 2012) also demonstrated that more altered (rehydrated) obsidian samples with higher volatile content tend to yield lower paleointensity values. In these latter two cases, the elevated water content appears to be associated with a secondary rehydration, and the interpretation was that the remanence was a TCRM associated with the alteration.

In the base of the TC Tuff, however, the increased LOI may be related to incomplete degassing, as opposed to secondary rehydration. Studies have consistently suggested a water-saturated magma source, with 4–6 wt% water (Lipman, 1966, 1971; Tefend et al., 2007; Warren et al., 1989), which closely corresponds to the

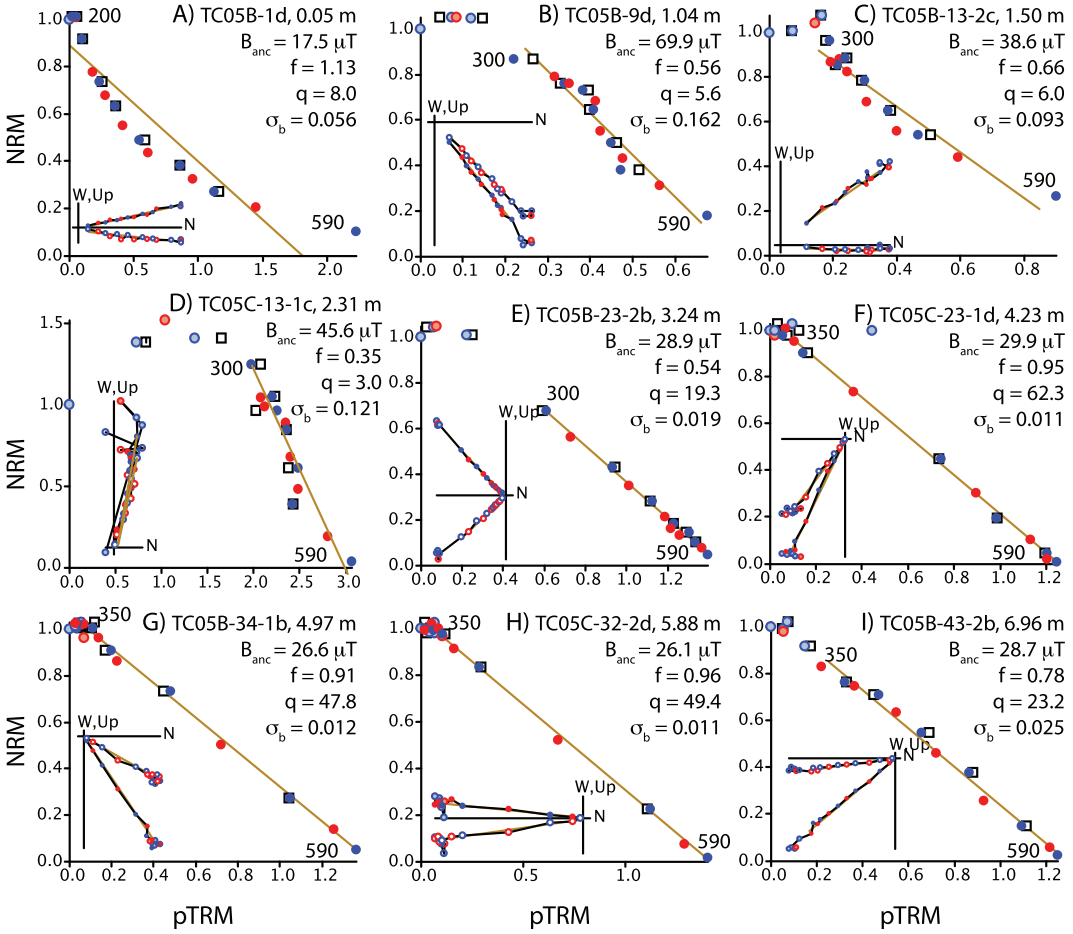

Figure 6. Representative Arai (NRM-pTRM) plots. Insets are NRM vector endpoint plots. Blue circles are zero-field and in-field (ZI) steps. Red circles are in-field and zero-field (IZ) steps. Lighter shading indicates points not used in slope calculation. Squares are pTRM checks. Temperatures of first and last points used in slope calculation shown. (a–d) were not used in final paleointensity estimate. (e–i) were used in final paleointensity interpretation.

maximum LOI we observe. We suggest that the increasing LOI near the base of the flow results from a basal zone that cooled quickly before complete degassing. In contrast, the less porous, densely welded flow interior (not sampled here) cooled more slowly, leading to a more complete degassing, and it is this degassed interior that experienced the most intensive devitrification and vapor-phase alteration (Rautman & Engstrom, 1996).

Additionally, while both LOI and paleointensity decrease upsection, the correlation is less than perfect. For example, the stable SD samples near 4.2 m and the SP/SD samples near 2.0 m have nearly identical LOI (~3%), but very different paleointensity behavior. The transition from low-quality to high-quality paleointensity results at ~3.24 m is not associated with dramatic changes in LOI. This leads us to conclude that the elevated water contents are not directly associated with paleointensity performance.

Even if the elevated LOI content is linked to incomplete degassing, as opposed to secondary rehydration, we cannot completely exclude the possibility that the NRM of some specimens may be a mixture of thermal and chemical remanences. The Tpcpv zone has experienced at least weak vapor-phase alteration, and if this resulted in a modification of the magnetic mineral assemblage, the paleointensity estimate could be affected. Experimentally, CRM will underestimate the paleointensity when it is treated as TRM (Draeger et al., 2006). Theoretically, underestimation of paleointensity is also caused by a CRM due to isothermal SD grain growth (Fabian, 2009). By contrast, dissolution of the magnetominerals and/or low-temperature oxidation after TRM acquisition can lead to a paleointensity overestimation (Fabian, 2009). Theoretically, TCRM in both

cases have straight Arai plots (Fabian, 2009), and both Ferk et al. (2011) and Avery et al. (2018) have shown that a likely TCRM can result in paleointensity results of high technical quality.

In our case, the presence of hematite at the base of section B may be from secondary alteration during cooling. However, the fact that samples from section C which lack hematite display nearly identical paleointensity behavior and results suggests that the remanence carried by magnetite was not affected. The described magnetite mineralogy (Jackson et al., 2006; Rosenbaum, 1986, 1993; Schlinger et al., 1988, 1991; Till et al., 2011; Worm & Jackson, 1999) varies consistently upsection only in grain size and shape in a way that is linked to natural cooling rate variations and not to spatially heterogeneous vapor-phase alteration.

It is more difficult to constrain the temperature at which the primary grain growth halted, however. Schlinger et al. (1991) suggest that the needle shape of the grains may arise from growth at $T < T_c$, which should lead to an underestimate of paleofield (Fabian, 2009). While some grain growth may have occurred at $T < T_c$, it is unlikely to have continued much below 500 °C, based on expected glass transition temperatures (section 2.1). This is especially true in the upper part of the section with low water contents which should be linked to higher glass transition temperatures. Results from Draeger et al. (2006) suggest that underestimates are slight (<10%) for TCRM acquired $T > 500$ °C. This suggests that the remanence acquired in the upper part of the section is largely a TRM or may be only very slightly biased by a TCRM.

We therefore conclude that our best estimate for the paleointensity comes from the stable SD samples in the moderately welded Tpcpv2 subzone, where grain growth likely ceased at $T > 500$ °C. Although weakly vapor-phase altered pumice clasts can be seen locally in this subzone, the majority of the matrix is not affected (Buesch et al., 1996; Chipera et al., 1995; Rautman & Engstrom, 1996; Sykes et al., 1979). This section of the TC Tuff with density ≥ 1.6 Mg/m^3 produces a mean cooling rate corrected value of 28.5 ± 1.94 μT and a VADM of 51.3 ZAm^2 at a paleolatitude of 36.8°N.

6.2. Uncertainties in Cooling Rate Correction

Another point of consideration is the uncertainty in the cooling rate correction. By assuming purely conductive cooling, we neglect any advective, hydrothermal cooling which would decrease cooling times. An additional uncertainty is introduced by the emplacement temperature selection. The exact emplacement temperature of the TC Tuff is unknown, and we choose to use 800 °C, the higher end of estimated emplacement temperatures. Halgedahl et al. (1980) and Fox and Aitken (1980) suggest that each order of magnitude decrease in cooling rate will result in a 5% overestimation in the paleointensity for SD grains. This corresponds to an average ~2.5% greater correction for emplacement at 800 °C compared to emplacement at 650 °C (lower end of estimated emplacement temperatures). In turn, this leads to an average ~0.8 μT less final paleointensity estimate.

6.3. Anomaly in the Linearity Test

A final question to tackle is the linearity of the magnetic minerals in the specimens. The decreased magnetization at 40 μT is not a typical nonlinear behavior described by Selkin et al. (2007), which shows a concave magnetization trend with the increasing field. We speculate that the deviation was caused by the human error during the laboratory measurements.

7. Conclusions

The Miocene TC Tuff samples from Yucca Mountain provide a unique opportunity to assess domain state effects on paleointensity estimates. The systematic variation in grain size from SP to stable SD allows us to isolate relatively narrow grain-size fractions. We find that the largest, stable SD samples with high average blocking temperatures result in high-quality paleointensity data with a well-defined cooling rate corrected average of 28.5 ± 1.94 μT (VADM of 51.3 ZAm^2). By contrast, the samples with lower blocking temperatures characteristic of smaller SD or SP/SD samples produce lower-quality results with higher and more scattered paleointensity values. This difference is not easily explained by Néel theory alone, but the link between paleointensity result and domain state is stronger than correlations with water content or other evidence

of alteration. Samples with grain-size distributions that contain a significant population of near-SP particles may not therefore be suitable paleointensity carriers.

The cooling history of the TC Tuff plays an important role in acquiring internally consistent and stable paleointensity estimation as this history and other rock magnetic properties are closely tied to stratigraphic height. However, care should be taken in identifying potential post-emplacement alteration below T_c as samples linked to SP behavior have consistently higher paleointensity and less ideal behavior. Given the potential spatial variability in cooling and alteration activity, a thorough evaluation of how magnetic mineralogy, cooling history, emplacement temperature, and alteration may control paleointensity is in order.

Acknowledgments
We thank the reviewers P. Doubrovine and G. Paterson for their thoughtful comments that helped improve this manuscript. We are grateful to the Institute for Rock Magnetism – Summer School in Rock Magnetism (SSRM) Students (SSRM Class of 2011), as well as John Bowar, for conducting the rock magnetic measurements. Thanks to Peter Solheid, Ramon Egli, and Brian Carter-Stiglitz for field work and sample collection. MacThellier paleointensity software was provided by Jeff Gee. This work was supported by the University of Wisconsin-Milwaukee Research and Growth Initiative and National Science Foundation Grant 1547483 to JB. Data associated with this paper can be found in the Magnetics Information Consortium (MagIC) database at earthref.org/MagIC/16705.

References

Avery, M. S., Gee, J. S., Bowles, J. A., & Jackson, M. J. (2018). Paleointensity estimates from ignimbrites: The Bishop Tuff revisited. *Geochemistry, Geophysics, Geosystems*, *19*(10), 3811–3831. https://doi.org/10.1029/2018gc007665

Bowles, J. A., Gee, J. S., Burgess, K., & Cooper, R. F. (2011). Timing of magnetite formation in basaltic glass: Insights from synthetic analogs and relevance for geomagnetic paleointensity analyses. *Geochemistry, Geophysics, Geosystems*, *12*(2), 1–18. https://doi.org/10.1029/2010GC003404

Bowles, J. A., Gee, J. S., Jackson, M. J., & Avery, M. S. (2015). Geomagnetic paleointensity in historical pyroclastic density currents: Testing the effects of emplacement temperature and postemplacement alteration. *Geochemistry, Geophysics, Geosystems*, *16*(10), 3607–3625. https://doi.org/10.1002/2015gc005910

Brodsky, N. S., Riggins, M., Connolly, J., & Ricci, P. (1997). *Thermal expansion, thermal conductivity, and heat capacity measurements for boreholes UE25 NRG-4, UE25 NRG-5, USW NRG-6, and USW NRG-7/7A* (No. SAND--95-1955). Albuquerque, NM (United States): Sandia National Labs.

Buesch, D. C., Spengler, R. W., Moyer, T. C., & Geslin, J. K. (1996). *Proposed stratigraphic nomenclature and macroscopic identification of lithostratigraphic units of the Paintbrush Group exposed at Yucca Mountain, Nevada* (No. DOE/NV/10874--T4; USGS-OFR--94-469). Las Vegas, NV (United States): USDOE Nevada Operations Office.

Byers Jr, F. M., Carr, W. J., Christiansen, R. L., Lipman, P. W., Orkild, P. P., & Quinlivan, W. D. (1976). *Geologic map of the Timber Mountain caldera area, Nye County, Nevada* (No. 891).

Byers, F. M., Carr, W. J., & Orkild, P. P. (1989). Volcanic centers of southwestern Nevada: Evolution of understanding, 1960–1988. *Journal of Geophysical Research - Solid Earth*, *94*(B5), 5908–5924. https://doi.org/10.1029/jb094ib05p05908

Chipera, S. J., Vaniman, D. T., Carlos, B. A., & Bish, D. L. (1995). *Mineralogic variation in drill core UE-25 UZ {number_sign} 16, Yucca Mountain, Nevada* (No. LA-12810-MS). NM (United States): Los Alamos National Lab.

Coe, R. S., Grommé, S., & Mankinen, E. A. (1978). Geomagnetic paleointensities from radiocarbon-dated lava flows on Hawaii and the question of the Pacific nondipole low. *Journal of Geophysical Research - Solid Earth*, *83*(B4), 1740–1756. https://doi.org/10.1029/jb083ib04p01740

Draeger, U., Prévot, M., Poidras, T., & Riisager, J. (2006). Single-domain chemical, thermochemical and thermal remanences in a basaltic rock. *Geophysical Journal International*, *166*(1), 12–32. https://doi.org/10.1111/j.1365-246x.2006.02862.x

Egli, R., & Lowrie, W. (2002). Anhysteretic remanent magnetization of fine magnetic particles. *Journal of Geophysical Research - Solid Earth*, *107*(B10). https://doi.org/10.1029/2001jb000671

Fabian, K. (2009). Thermochemical remanence acquisition in single-domain particle ensembles: A case for possible overestimation of the geomagnetic paleointensity. *Geochemistry, Geophysics, Geosystems*, *10*(6). https://doi.org/10.1029/2009gc002420

Ferk, A., Denton, J. S., Leonhardt, R., Tuffen, H., Koch, S., Hess, K. U., & Dingwell, D. B. (2012). Paleointensity on volcanic glass of varying hydration states. *Physics of the Earth and Planetary Interiors*, *208*, 25–37. https://doi.org/10.1016/j.pepi.2012.06.004

Ferk, A., Leonhardt, R., Aulock, F. V., Hess, K. U., & Dingwell, D. B. (2011). Paleointensities of phonolitic obsidian: Influence of emplacement rotations and devitrification. *Journal of Geophysical Research - Solid Earth*, *116*(B12). https://doi.org/10.1029/2011jb008397

Flint, A. L., Flint, L. E., Bodvarsson, G. S., Kwicklis, E. M., & Fabryka-Martin, J. (2001). Evolution of the conceptual model of unsaturated zone hydrology at Yucca Mountain, Nevada. *Journal of Hydrology*, *247*(1-2), 1–30. https://doi.org/10.1016/s0022-1694(01)00358-4

Flood, T. P. (1987). *Cyclic evolution of a magmatic system: The Paintbrush Tuff, SW Nevada volcanic field (Doctoral dissertation, Michigan State University. Department of Geological Science)*.

Fox, J. M. W., & Aitken, M. J. (1980). Cooling-rate dependence of thermoremanent magnetisation. *Nature*, *283*(5746), 462. https://doi.org/10.1038/283462a0

Frizzell Jr, V. A., & Shulters, J. (1990). *Geologic map of the Nevada test site, southern Nevada* (No. 2046).

Gee, J. S., & Kent, D. V. (2007). Source of oceanic magnetic anomalies and the geomagnetic polarity time scale. *Treatise on Geophysics*, 455–507. https://doi.org/10.1016/b978-044452748-6.00097-3

Gibson, J. D., Swan, F. H., Wesling, J. R., Bullard, T. F., Perman, R. C., Angell, M. M., & DiSilvestro, L. A. (1992). *Summary and evaluation of existing geological and geophysical data near prospective surface facilities in Midway Valley, Yucca Mountain Project, Nye County, Nevada; Yucca Mountain Site Characterization Project* (No. SAND--90-2491). Albuquerque, NM (United States): Sandia National Labs.

Giordano, D., Nichols, A. R., & Dingwell, D. B. (2005). Glass transition temperatures of natural hydrous melts: A relationship with shear viscosity and implications for the welding process. *Journal of Volcanology and Geothermal Research*, *142*(1-2), 105–118. https://doi.org/10.1016/j.jvolgeores.2004.10.015

Grunder, A. L., Laporte, D., & Druitt, T. H. (2005). Experimental and textural investigation of welding: Effects of compaction, sintering, and vapor-phase crystallization in the rhyolitic Rattlesnake Tuff. *Journal of Volcanology and Geothermal Research*, *142*(1-2), 89–104. https://doi.org/10.1016/j.jvolgeores.2004.10.018

Halgedahl, S. L., Day, R., & Fuller, M. (1980). The effect of cooling rate on the intensity of weak-field TRM in single-domain magnetite. *Journal of Geophysical Research - Solid Earth*, *85*(B7), 3690–3698. https://doi.org/10.1029/jb085ib07p03690

Istok, J. D., Rautman, C. A., Flint, L. E., & Flint, A. L. (1994). Spatial variability in hydrologic properties of a volcanic tuff. *Groundwater*, *32*(5), 751–760. https://doi.org/10.1111/j.1745-6584.1994.tb00916.x

Jackson, M., Carter-Stiglitz, B., Egli, R., & Solheid, P. (2006). Characterizing the superparamagnetic grain distribution f (V, Hk) by thermal fluctuation tomography. *Journal of Geophysical Research - Solid Earth*, *111*(B12). https://doi.org/10.1029/2006jb004514

Jackson, M., & Solheid, P. (2010). On the quantitative analysis and evaluation of magnetic hysteresis data. *Geochemistry, Geophysics, Geosystems*, *11*(4). https://doi.org/10.1029/2009gc002932

Kirschvink, J. L. (1980). The least-squares line and plane and the analysis of palaeomagnetic data. *Geophysical Journal International*, *62*(3), 699–718.

Keefer, W. R., Whitney, J. W., & Buesch, D. C. (2007). Geology of the Yucca Mountain site area, southwestern Nevada. *Geological Society of America Memoirs*, *199*, 53. https://doi.org/10.1130/2007.1199(03)

Korte, M., & Constable, C. (2011). Improving geomagnetic field reconstructions for 0–3 ka. *Physics of the Earth and Planetary Interiors*, *188*, 247–259. https://doi.org/10.1016/j.pepi.2011.06.017

Lavallée, Y., Wadsworth, F. B., Vasseur, J., Russell, J. K., Andrews, G. D., Hess, K. U., et al. (2015). Eruption and emplacement timescales of ignimbrite super-eruptions from thermo-kinetics of glass shards. *Frontiers in Earth Science*, *3*, 2. https://doi.org/10.3389/feart.2015.00002

Levy, S. S., Norman, D. I., & Chipera, S. J. (1995). Alteration history studies in the exploratory studies facility, Yucca Mountain, Nevada, USA. MRS Online Proceedings Library Archive, 412.

Lipman, P. W. (1966). Water pressures during differentiation and crystallization of some ash-flow magmas from southern Nevada. *American Journal of Science*, *264*(10), 810–826. https://doi.org/10.2475/ajs.264.10.810

Lipman, P. W. (1971). Iron-titanium oxide phenocrysts in compositionally zoned ash-flow sheets from southern Nevada. *The Journal of Geology*, *79*(4), 438–456. https://doi.org/10.1086/627651

Moyer, T. C., Geslin, J. K., & Flint, L. E. (1997). *Stratigraphic relations and hydrologic properties of the Paintbrush Tuff nonwelded (PTn) hydrologic unit, Yucca Mountain, Nevada* (No. Report 95-397). Las Vegas, Nevada (US): Yucca Mountain Project.

Pullaiah, G., Irving, E., Buchan, K. L., & Dunlop, D. J. (1975). Magnetization changes caused by burial and uplift. *Earth and Planetary Science Letters*, *28*(2), 133–143. https://doi.org/10.1016/0012-821x(75)90221-6

Rautman, C. A., & Engstrom, D. A. (1996). *Geology of the USW SD-12 drill hole Yucca Mountain, Nevada* (No. SAND--96-1368). Albuquerque, NM (United States): Sandia National Labs.

Riehle, J. R. (1973). Calculated compaction profiles of rhyolitic ash-flow tuffs. *Geological Society of America Bulletin*, *84*(7), 2193–2216. https://doi.org/10.1130/0016-7606(1973)84<2193:ccpora>2.0.co;2

Rosenbaum, J. G. (1986). Paleomagnetic directional dispersion produced by plastic deformation in a thick Miocene welded tuff, southern Nevada: Implications for welding temperatures. *Journal of Geophysical Research - Solid Earth*, *91*(B12), 12817–12834. https://doi.org/10.1029/jb091ib12p12817

Rosenbaum, J. G. (1993). Magnetic grain-size variations through an ash flow sheet: Influence on magnetic properties and implications for cooling history. *Journal of Geophysical Research - Solid Earth*, *98*(B7), 11715–11727. https://doi.org/10.1029/93jb00355

Rosenbaum, J. G., Hudson, M. R., & Scott, R. B. (1991). Paleomagnetic constraints on the geometry and timing of deformation at Yucca Mountain, Nevada. *Journal of Geophysical Research - Solid Earth*, *96*(B2), 1963–1979. https://doi.org/10.1029/90jb01966

Rosenbaum, J. G., & Rivers, W. C. (1984). *Paleomagnetic orientation of core from drill hole USW GU-3 Yucca Mountain, Nevada: Tiva Canyon Member of the Paintbrush Tuff* (No. USGS-OFR-85-48). Denver, CO (United States): Geological Survey.

Rosenbaum, J. G., & Snyder, D. B. (1984). *Preliminary interpretation of paleomagnetic and magnetic property data from drill holes USW G-1, G-2, GU-3, G-3, and VH-1 and surface localities in the vicinity of Yucca Mountain, Nye County, Nevada* (No. USGS-OFR--85-49). Denver, CO (United States): Geological Survey.

Sawyer, D. A., Fleck, R. J., Lanphere, M. A., Warren, R. G., Broxton, D. E., & Hudson, M. R. (1994). Episodic caldera volcanism in the Miocene southwestern Nevada volcanic field: Revised stratigraphic framework, 40Ar/39Ar geochronology, and implications for magmatism and extension. *Geological Society of America Bulletin*, *106*(10), 1304–1318. https://doi.org/10.1130/0016-7606(1994)106<1304:ecvitm>2.3.co;2

Schlinger, C. M., Rosenbaum, J. G., & Veblen, D. R. (1988). Fe-oxide microcrystals in welded tuff from southern Nevada: Origin of remanence carriers by precipitation in volcanic glass. *Geology*, *16*(6), 556–559. https://doi.org/10.1130/0091-7613(1988)016<0556:fomiwt>2.3.co;2

Schlinger, C. M., Veblen, D. R., & Rosenbaum, J. G. (1991). Magnetism and magnetic mineralogy of ash flow tuffs from Yucca Mountain, Nevada. *Journal of Geophysical Research - Solid Earth*, *96*(B4), 6035–6052. https://doi.org/10.1029/90jb02653

Selkin, P. A., Gee, J. S., & Tauxe, L. (2007). Nonlinear thermoremanence acquisition and implications for paleointensity data. *Earth and Planetary Science Letters*, *256*(1-2), 81–89. https://doi.org/10.1016/j.epsl.2007.01.017

Selkin, P. A., & Tauxe, L. (2000). Long-term variations in palaeointensity. *Philosophical Transactions of the Royal Society of London, Series A: Mathematical, Physical and Engineering Sciences*, *358*(1768), 1065–1088. https://doi.org/10.1098/rsta.2000.0574

Sheridan, M. F., & Ragan, D. M. (1975). Compaction of ash-flow tuffs. In *Compaction of Coarse-Grained Sediments* (pp. 677–717). https://doi.org/10.1016/s0070-4571(08)71103-8

Sykes, M. L., Heiken, G. H., & Smyth, J. R. (1979). *Mineralogy and petrology of tuff units from a UE25a-1 drill site, Yucca Mountain, Nevada* (No. LA--8139-MS). NM (United States): Los Alamos Scientific Lab.

Tauxe, L., & Staudigel, H. (2004). Strength of the geomagnetic field in the Cretaceous Normal Superchron: New data from submarine basaltic glass of the Troodos Ophiolite. *Geochemistry, Geophysics, Geosystems*, *5*(2). https://doi.org/10.1029/2003gc000635

Tefend, K. S., Vogel, T. A., Flood, T. P., & Ehrlich, R. (2007). Identifying relationships among silicic magma batches by polytopic vector analysis: A study of the Topopah Spring and Pah Canyon ash-flow sheets of the southwest Nevada volcanic field. *Journal of Volcanology and Geothermal Research*, *167*(1-4), 198–211. https://doi.org/10.1016/j.jvolgeores.2006.07.011

Thellier, E. (1959). Sur l'intensite du champ magnetique terrestre dans le passe historique et goologique. *Annales de Geophysique*, *15*, 285–376.

Thompson, R., & Oldfield, F. (1986). *Environmental magnetism*. London: Allen & Unwin. 227 pp.

Till, J. L., Jackson, M. J., Rosenbaum, J. G., & Solheid, P. (2011). Magnetic properties in an ash flow tuff with continuous grain size variation: A natural reference for magnetic particle granulometry. *Geochemistry, Geophysics, Geosystems*, *12*(7). https://doi.org/10.1029/2011gc003648

Turcotte, D. L., & Schubert, G. (2002). *Geodynamics*. Cambridge: England, UK.

Warren, R. G., Byers, F. M., Broxton, D. E., Freeman, S. H., & Hagan, R. C. (1989). Phenocryst abundances and glass and phenocryst compositions as indicators of magmatic environments of large-volume ash flow sheets in southwestern Nevada. *Journal of Geophysical Research - Solid Earth*, *94*(B5), 5987–6020. https://doi.org/10.1029/jb094ib05p05987

Worm, H. U., & Jackson, M. (1999). The superparamagnetism of Yucca Mountain tuff. *Journal of Geophysical Research - Solid Earth*, *104*(B11), 25415–25425. https://doi.org/10.1029/1999jb900285